

Numerical study of plume patterns in a chemotaxis–diffusion–convection coupling system



Yannick Deleuze^{a,b,*}, Chen-Yu Chiang^b, Marc Thiriet^{a,c,d}, Tony W.H. Sheu^{b,e}

^a Sorbonne Universités, UPMC Univ Paris 06, UMR 7598, Laboratoire Jacques-Louis Lions, Paris F-75005 France

^b Department of Engineering Science and Ocean Engineering, National Taiwan University, No. 1, Sec. 4, Roosevelt Road, Taipei, Taiwan

^c CNRS, UMR 7598, Laboratoire Jacques-Louis Lions, Paris F-75005 France

^d INRIA-Paris-Rocquencourt, EPC REO, Domaine de Voluceau, BP105, 78153 Le Chesnay Cedex, France

^e Center for Advanced Study in Theoretical Sciences, National Taiwan University, No. 1, Sec. 4, Roosevelt Road, Taipei, Taiwan

ARTICLE INFO

Article history:

Received 15 December 2014

Revised 21 October 2015

Accepted 26 October 2015

Available online 2 December 2015

Keywords:

Chemotaxis

Finite element method

Incompressible viscous fluid flow

Coupled KS–NS

ABSTRACT

A chemotaxis–diffusion–convection coupling system for describing a form of buoyant convection in which the fluid develops convection cells and plume patterns will be investigated numerically in this study. Based on the two-dimensional convective chemotaxis–fluid model proposed in the literature, we developed an up-wind finite element method to investigate the pattern formation and the hydrodynamical stability of the system. The numerical simulations illustrate different predicted physical regimes in the system. In the convective regime, the predicted plumes resemble Bénard instabilities. Our numerical results show how structured layers of bacteria are formed before bacterium rich plumes fall in the fluid. The plumes have a well defined spectrum of wavelengths and have an exponential growth rate, yet their positions can only be predicted in very simple examples. In the chemotactic and diffusive regimes, the effects of chemotaxis are investigated. Our results indicate that the chemotaxis can stabilize the overall system. A time scale analysis has been performed to demonstrate that the critical taxis Rayleigh number for which instabilities set in depends on the chemotaxis head and sensitivity. In addition, the comparison of the differential systems of chemotaxis–diffusion–convection, double diffusive convection, and Rayleigh–Bénard convection establishes a set of evidences that even if the physical mechanisms are different at the same time the PDE systems share similarities.

© 2015 Elsevier Ltd. All rights reserved.

1. Introduction

Taxis refers to the collective motion of cells or an organism in response to an attractant gradient. The nature of the attractant stimulus can be of chemical (chemotaxis), physical (baro-, electro-, magneto-, phono-, photo-, and thermotaxis), or mechanical (gyro-, hacto-, and rheotaxis) origins. Chemotaxis refers to cell movement primed by an external chemical signal that can either be emitted by the same population of cells or created by an external source [1]. In particular, aerotaxis is related to the movement toward a gradient of increasing oxygen concentration.

The phenomenon that couples chemotaxis, diffusion, and convection has been illustrated by experiments on suspensions of bacteria

in a container filled with water [2,3]. Oxygen diffuses in the container from the surface. As bacteria consume oxygen, oxygen concentration falls everywhere except at the surface, hence creating a vertical concentration difference. Bacteria move up to higher concentration of oxygen and quickly get densely packed below the surface in a relatively thin layer. Subsequently, Rayleigh–Bénard-like instability appears near the surface. These dynamical instabilities exhibit complex convection patterns with plumes of bacteria falling in the fluid.

Chemotaxis–diffusion–convection is a particular case of the so-called bioconvection. Bioconvection is a more general term for suspensions of swimming microorganisms which are denser than the solvent fluid. Bioconvection and the different mechanisms of up-swimming have been reviewed [4].

Mathematical modeling of chemotaxis has been introduced by authors in [5,6]. Mathematical analysis mainly focused on pattern formation of microorganisms and blow-up phenomena in finite time. Key contributions on chemotactic collapse have been brought by authors in [7–12]. Similarly, angiogenesis is the motion of endothelial cells to form new blood vessels from preexisting vessels to locally supply oxygen. During tumor growth, tumor cells secrete a set of

* Corresponding author at: Department of Engineering Science and Ocean Engineering, National Taiwan University, No. 1, Sec. 4, Roosevelt Road, Taipei, Taiwan. Tel.: +886 2 33665746; fax: +886 2 23929885.

E-mail addresses: yannick.deleuze@ljl.math.upmc.fr, d01525014@ntu.edu.tw (Y. Deleuze), f01525007@ntu.edu.tw (C.-Y. Chiang), marc.thiriet@upmc.fr (M. Thiriet), twshsheu@ntu.edu.tw (T.W.H. Sheu).

Table 1
Nomenclature description.

Parameter	Definition	Dimension
c	Concentration of oxygen	mol
c_{air}	Concentration of oxygen in air	mol
D	Diffusivity	$\text{m}^2 \text{s}^{-1}$
h	Container height	m
H	Chemotaxis head	
\mathbf{j}	Vertical unit vector upwards	
ℓ	Dimensionless half container width	
Le	Lewis number	
n	Number density of bacteria	m^{-3}
\mathbf{n}	Unit outward normal vector	
n_0	Initial number density of bacteria	m^{-3}
\bar{n}_0	Initial average number density of bacteria	m^{-3}
p	Pressure	kg m s^{-2}
Pr	Prandtl number	
Ra	Rayleigh number	
S	Dimensionless chemotaxis sensitivity	
S_{dim}	Dimensional chemotaxis sensitivity	$\text{m}^5 \text{s}^{-1} \text{mol}^{-1}$
s	Solute concentration	mol
t	Time	s
T	Time scale of bacterium transport	s
T	Temperature	K
$\mathbf{u} = (u, v)$	Velocity vector	m s^{-1}
V_b	Volume of a bacterium	m^3
$\mathbf{x} = (x, y)$	Coordinate axes	m
Greek symbols		
β_s	Solute expansion coefficient	mol^{-1}
β_T	Thermal expansion coefficient	K^{-1}
κ	Bacterium oxygen consumption rate	s^{-1}
μ	Dynamic viscosity	$\text{kg m}^{-1} \text{s}^{-1}$
ν	Kinematic viscosity	$\text{m}^2 \text{s}^{-1}$
ρ	Fluid density	kg m^{-3}
ρ_b	Bacterium volumetric mass density	kg m^{-3}
Subscripts		
\cdot_b	Bacterium	
\cdot_{conv}	Convection	
\cdot_{diff}	Diffusion	
\cdot_m	Mass	
\cdot_o	Oxygen	
\cdot_τ	Taxis	
\cdot_T	Thermal	

substances to attract endothelial cells [13,14]. In angiogenesis models, chemotactic collapse was not observed [15,16]. In this study, the model equations (1)–(4) are used to describe the chemotaxis response of bacterial suspensions. An unstable agglomeration of bacterial cells at the surface leads to a descent of cell-rich plume patterns together with the formation of high-speed jets between counter-rotating vortices.

Formation and stability of plumes result from the balance between chemotaxis, diffusion, and convection of bacteria. The particular impact of each mechanism still needs to be understood. Chemotaxis is known to bring instability in system and leads to aggregation, but may also have a stabilizing effect. The stability of plumes also requires oxygen inflow and diffusion.

The linear stability analysis of the chemotaxis–diffusion–convection system showed that a condition for linear instability depends on the taxis Rayleigh number Ra_τ [2]. The taxis Rayleigh number is defined as the ratio of buoyancy and viscosity forces times the ratio of momentum and cell diffusivity. Below a critical value ($Ra_\tau < Ra_c$), then the process remains stable. From experiments, several stages were observed starting from the upward bacteria accumulation and leading to hydrodynamic formation of plumes. A weakly nonlinear stability analysis was conducted to investigate the stability of hexagon and roll patterns formed by the system of Eqs. (1)–(4) [17]. The hydrodynamic vortices formed by convection strengthen circulation of fluid and enhance the intake of oxygen into the solvent [18]. Global existence for the chemotaxis–Stokes system for small ini-

tial bacterial population density was proved in [19]. Then, global existence for the chemotaxis–Navier–Stokes system for a large initial bacterial population density as well as global existence of 3D weak solutions for the chemotaxis–Stokes equations were proved in [20].

A detailed numerical study of the plume formation and merging that was related to the convergence of Rayleigh–Bénard-type patterns was carried out in [21]. The shape and number of plumes can be controlled by initial bacterial population density. However, the sites of plumes have not been predicted. The convergence toward numerically stable stationary plumes for low and high initial density of cells is revealed in [21].

In this paper, a computational model based on the finite element method is proposed aiming at investigating the behavior of the two-dimensional chemotaxis–diffusion–convection system. We present numerical examples of different states of the system: (i) diffusion dominant, (ii) chemotaxis dominant, and (iii) convection dominant with the formation of descending plumes. Furthermore, we show that the chemotaxis sensitivity (S) and the taxis Rayleigh number (Ra_τ) are two relevant parameters for the generation of instabilities (Table 1). The effects of initial conditions and the initial cell density were also explored. Distinct initial settings lead to different solutions with plume patterns. Numerical tests show how the specified deterministic initial condition influences the overall behavior such as the number of plumes. In addition, the chemotaxis–diffusion–convection system is compared with the Rayleigh–Bénard and double-diffuse convection systems. The dimensionless parameters introduced in previous papers were renamed for better readability (Table 2).

In Section 2 of the present paper, the mathematical formulation of the chemotaxis–diffusion–convection system is presented. Section 3 gives the numerical method. Section 4 demonstrates the role of chemotaxis, in addition to a discussion on the simulation results and comparison with other models of buoyant convection. Finally, Section 5 presents some concluding remarks.

2. Mathematical model

A mathematical model for the chemotaxis–diffusion–convection is proposed in [3] and reads as follows:

$$\rho \left(\frac{\partial \mathbf{u}}{\partial t} + \mathbf{u} \cdot \nabla \mathbf{u} \right) + \nabla p - \mu \nabla^2 \mathbf{u} = -n V_b g (\rho_b - \rho) \mathbf{j}, \quad (1)$$

$$\nabla \cdot \mathbf{u} = 0, \quad (2)$$

$$\frac{\partial n}{\partial t} + \nabla \cdot [\mathbf{u} n - D_b \nabla n + S_{\text{dim}} r(c) n \nabla c] = 0, \quad (3)$$

$$\frac{\partial c}{\partial t} + \nabla \cdot (\mathbf{u} c - D_o \nabla c) = -n \kappa r(c), \quad (4)$$

where $\mathbf{u} = (u, v)$ denotes the velocity field of water (solvent), p the pressure, ρ and μ the water density and viscosity, n the areal number density of bacteria (i.e., number of bacteria per unit area in a 2D space), V_b and ρ_b the volume and volumetric mass density of a bacterium, c the concentration of oxygen, $V_b g (\rho_b - \rho) \mathbf{j}$ the buoyancy force exerted by a bacterium on the fluid in the vertical direction (unit vector \mathbf{j}), S_{dim} the dimensional chemotaxis sensitivity, D_b and D_o the bacterium and oxygen diffusivities, κ the bacterial oxygen consumption rate, and $r(c)$ the dimensionless cut-off function for oxygen concentration. The cut-off function $r(c)$ is defined by the step function

$$r(c) = \begin{cases} 1 & \text{if } c > c^*, \\ 0 & \text{if } c \leq c^*, \end{cases} \quad (5)$$

where $c^* = 0.3$.

Table 2

Representative dimensionless numbers involved in the double diffusive convection (DDC) system (26), chemotaxis–diffusion–convection (CDC) system (10), and Rayleigh–Bénard convection (RBC) system (27). Subscripts $\cdot_m, \cdot_T, \cdot_\tau, \cdot_s, \cdot_o, \cdot_b$ stand for mass, thermal, taxis, solute, oxygen, and bacterium, respectively; g is the acceleration due to gravity; β_T and β_s are the coefficients for thermal and solute expansion, respectively; ν is the kinematic viscosity. Note that only the CDC system denotes parameters of the considered system (10).

	DDC	CDC	RBC
Rayleigh number	$Ra_T = \frac{g \beta_T \Delta T L^3}{D_T \nu}$ $Ra_m = \frac{g \beta_s \Delta s L^3}{D_s \nu}$	$Ra_\tau = \frac{g V_b \bar{n}_0 (\rho_b - \rho) L^3}{D_b \mu}$	$Ra_T = \frac{g \beta_T \Delta T L^3}{D_T \mu}$
Prandtl number	$Pr_T = \frac{\nu}{D_T}$	$Pr_\tau = \frac{\nu}{D_b}$	$Pr_T = \frac{\nu}{D_T}$
Lewis number	$Le_T = \frac{D_T}{D_s}$	$Le_\tau = \frac{D_o}{D_b}$	
Chemotaxis sensitivity		$S = \frac{S_{\text{dim}} c_{\text{air}}}{D_b}$	
Chemotaxis head		$H = \frac{\kappa \bar{n}_0 L^2}{c_{\text{air}} D_b}$	

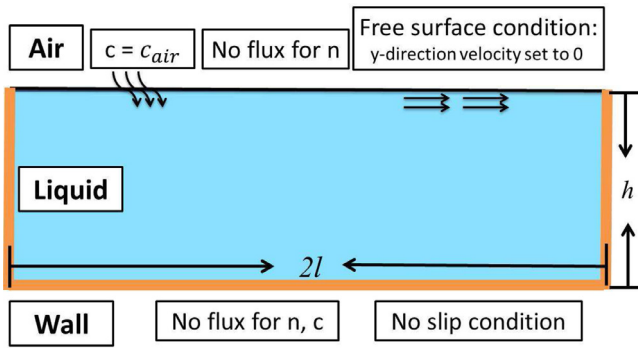


Fig. 1. Boundary conditions for the system of Eqs. (1)–(4). The air–water interface, where the oxygen concentration is equal to that of air, is not crossed by bacteria; the fluid vertical velocity component equals zero and the fluid is assumed to be free of tangential stress. The container walls are impermeable to bacteria and oxygen; a no-slip condition is imposed.

Bacteria are slightly denser than water and are diluted in the solvent, so that we consider $(\rho_b - \rho)/\rho \ll 1$ and $nV_b \ll 1$, respectively. The consumption of oxygen is proportional to the bacterial population density n . Both n and c are advected by the fluid. When the oxygen concentration is lower than a threshold, the bacteria become quiescent [3], that is, they neither consume oxygen nor swim toward sites of higher oxygen concentrations. The dynamics of space filling, intercellular signaling, and quorum sensing are also neglected.

The system of Eqs. (1)–(4) with the boundary conditions introduced in previous papers (e.g. [2,18,21]) is solved in a two-dimensional rectangular container (Ω). The top boundary (Γ_{top}) represents the interface between liquid and air. On the free surface the concentration of oxygen is equal to the air concentration of oxygen (c_{air}) and the free tangential stress condition as well as the absence of bacterial flux are prescribed (Fig. 1). Therefore,

$$\frac{\partial u}{\partial y} = 0, \quad v = 0, \quad c = c_{\text{air}}, \quad (6)$$

$$S_{\text{dim}} n r(c) \nabla c \cdot \mathbf{n} - D_b \nabla n \cdot \mathbf{n} = 0 \quad \text{on } \Gamma_{\text{top}},$$

where \mathbf{n} is the unit outward normal vector. On the container walls (Γ_w), a no-slip boundary condition is prescribed and the fluxes of bacteria and oxygen equal zero:

$$u = 0, \quad v = 0, \quad \nabla n \cdot \mathbf{n} = 0, \quad \nabla c \cdot \mathbf{n} = 0 \quad \text{on } \Gamma_w. \quad (7)$$

A no-slip condition at the air–water interface would enable the formation of hydrodynamic instabilities. The effect of a moving bound-

ary due to the advection caused by an incompressible fluid flow is to be explored.

3. Computational model

3.1. Scaling and setting for numerical simulations

The characteristic length is defined by the container height h and the characteristic bacterial density by the average of the initial bacterial population density defined as

$$\bar{n}_0 := \frac{1}{|\Omega|} \int_{\Omega} n_0(x, t) dx. \quad (8)$$

This particular choice of characteristic bacterial density allows us to easily measure the total number of bacteria in each simulation for different initial distributions of bacteria.

Dimensionless variables are defined as in [2,18,21]

$$\mathbf{x}' = \frac{\mathbf{x}}{h}, \quad t' = \frac{t}{h^2/D_b}, \quad n' = \frac{n}{\bar{n}_0}, \quad (9)$$

$$c' = \frac{c}{c_{\text{air}}}, \quad p' = \frac{p}{\mu D_b/h^2}, \quad \mathbf{u}' = \frac{\mathbf{u}}{D_b/h}.$$

Five dimensionless parameters given below characterize the hydrodynamic and chemotaxis transport equations:

$$Pr_\tau = \frac{\nu}{D_b}, \quad Ra_\tau = \frac{g V_b \bar{n}_0 (\rho_b - \rho) L^3}{D_b \mu}, \quad S = \frac{S_{\text{dim}} c_{\text{air}}}{D_b}, \quad (10)$$

$$H = \frac{\kappa \bar{n}_0 L^2}{c_{\text{air}} D_b}, \quad Le_\tau = \frac{D_o}{D_b}$$

where Pr_τ is the taxis Prandtl number, Ra_τ the taxis Rayleigh number (buoyancy-driven flow), Le_τ the taxis Lewis number, S the dimensionless chemotaxis sensitivity, and H the chemotaxis head. The chemotaxis head corresponds to the consumption of the chemoattractant by the bacteria. The taxis Prandtl, Rayleigh, and Lewis numbers are analogous to the respective heat and mass Prandtl, Rayleigh, and Lewis numbers in heat and mass transfer (Table 2). The chemotaxis sensitivity (S) and head (H) characterize the chemotaxis system. Only Ra_τ and H depend on the characteristic length L and characteristic bacterial density \bar{n}_0 .

After removing the prime in dimensionless quantities, the set of dimensionless equations becomes

$$\begin{aligned} \frac{\partial \mathbf{u}}{\partial t} + \mathbf{u} \cdot \nabla \mathbf{u} - Pr_\tau \nabla^2 \mathbf{u} + Pr_\tau \nabla p &= -Ra_\tau Pr_\tau n \mathbf{j}, \\ \nabla \cdot \mathbf{u} &= 0, \\ \frac{\partial n}{\partial t} + \mathbf{u} \cdot \nabla n - \nabla^2 n + S \nabla \cdot (r(c)n \nabla c) &= 0, \\ \frac{\partial c}{\partial t} + \mathbf{u} \cdot \nabla c - Le_\tau \nabla^2 c &= Hnr(c). \end{aligned} \quad (11)$$

The system (10) is solved in a rectangular domain $\Omega = [-\ell, \ell] \times [0, 1]$ with the initial conditions:

$$\mathbf{u}(\mathbf{x}, 0) = \mathbf{u}_0(\mathbf{x}), \quad n(\mathbf{x}, 0) = n_0(\mathbf{x}), \quad c(\mathbf{x}, 0) = c_0(\mathbf{x}). \quad (12)$$

On the top of the domain Ω , the dimensionless boundary conditions are prescribed as

$$\frac{\partial u}{\partial y} = 0, \quad v = 0, \quad S r(c) n \nabla c \cdot \mathbf{n} - D_b \nabla n \cdot \mathbf{n} = 0, \quad c = 1, \quad (13)$$

while on the other boundaries, we impose the dimensionless boundary conditions as follows

$$u = 0, \quad v = 0, \quad \nabla n \cdot \mathbf{n} = 0, \quad \nabla c \cdot \mathbf{n} = 0. \quad (14)$$

In the following sections, we will refer to the hydrodynamic system for the first two equations in (11) and to the chemotaxis system for the last two equations in (11).

3.2. Numerical methods

The governing equations in (11) are solved using the finite element method. We adopt the biquadratic quadrilateral elements for the primitive variables \mathbf{u} and the bilinear quadrilateral elements for the primitive variables p so as to satisfy the LBB (Ladyžhenskaya [22]–Babuška [23]–Brezzi [24]) stability condition. There are nine nodes in one biquadratic quadrilateral element and four nodes in one bilinear quadrilateral element. In each element, the function ϕ can be written as $\phi = \sum_i N^i \phi_i$, where ϕ_i are the nodal unknowns.

To avoid the convective instability while solving the convection dominated flow equations and maintain accuracy, we adopt the idea of a streamline upwind/Petrov–Galerkin (SUPG) method [25]. We implemented an inconsistent Petrov–Galerkin weighted residual scheme such that the weighted residuals statement is kept biased in favor of the upstream flow direction by adding artificial viscosity of physical plausibility in Galerkin framework to the convection term [26–29]. The resulting weak formulation reads as

$$\begin{aligned} \int_\Omega \left[N \frac{\partial \phi}{\partial t} + W \left(u \frac{\partial \phi}{\partial x} + v \frac{\partial \phi}{\partial y} \right) + k \left(\frac{\partial N}{\partial x} \frac{\partial \phi}{\partial x} + \frac{\partial N}{\partial y} \frac{\partial \phi}{\partial y} \right) \right] d\Omega \\ = \int_\Omega f d\Omega + k \left(N \frac{\partial \phi}{\partial x} \Big|_{x_1}^{x_2} + N \frac{\partial \phi}{\partial y} \Big|_{y_1}^{y_2} \right). \end{aligned} \quad (15)$$

In the context of inconsistent formulation, we have two kinds of test functions. For the non-convective terms we choose the test function to be the shape function N . The test function W is only applied to the convective term so as to add a numerical stabilizing term. The main purpose of employing a SUPG scheme is to add an amount of streamline artificial viscosity. The test function W is therefore rewritten in two parts $W = N + B$. B is called the biased part. On each node i , the biased part is $B_j^i = \tau u_j \frac{\partial N^i}{\partial x_j}$ where $j \in \{1, 2\}$ corresponds to the Cartesian coordinates and $(u_1, u_2) = (u, v)$.

From the exact solution of the convection–diffusion equation in one dimension, following the derivation in [28], the constant τ , accounting for the amount of artificial viscosity to achieve stable and accurate solutions, is determined as [26–29]

$$\tau = \frac{\delta(\gamma_1) u h_1 + \delta(\gamma_2) v h_2}{2(u^2 + v^2)}. \quad (16)$$

We define $\gamma_j = \frac{u_j h_j}{2k}$ with $(h_1, h_2) = (\Delta x, \Delta y)$ being denoted as the grid sizes. Finally, the derived expression for $\delta(\gamma)$ is given below

$$\delta(\gamma) = \begin{cases} \frac{2 - \cosh(\gamma) - \frac{4}{\gamma} \tanh(\frac{\gamma}{2}) + \frac{1}{\gamma} \sinh(\gamma)}{4 \tanh(\frac{\gamma}{2}) - \sinh(\gamma) - \frac{6}{\gamma} \sinh(\gamma) \tanh(\frac{\gamma}{2})}, & \text{at end-nodes,} \\ \frac{1}{2} \coth\left(\frac{\gamma}{2}\right) - \frac{1}{\gamma}, & \text{at center-nodes.} \end{cases} \quad (17)$$

For comparison purpose in Section 4.4, the double diffusion system (26) and the Rayleigh–Bénard system (27) are solved using the software Freefem++ [30]. The code uses a finite element method based on the weak formulation of the problem. Taylor–Hood \mathbb{P}_2 – \mathbb{P}_1 elements are chosen in FreeFem++. These elements are used together with a characteristic/Galerkin formulation to stabilize the convection terms.

3.3. Numerical validation of the coupled NS–KS equations

In this validation study, the following dimensionless differential equations accounting for the coupled Keller–Segel and incompressible viscous hydrodynamic equations are solved

$$\begin{aligned} \frac{\partial \mathbf{u}}{\partial t} + \mathbf{u} \cdot \nabla \mathbf{u} - Pr_\tau \nabla^2 \mathbf{u} + Pr_\tau \nabla p &= -Ra_\tau Pr_\tau n \mathbf{j} + \mathbf{f}_u, \\ \nabla \cdot \mathbf{u} &= 0, \\ \frac{\partial n}{\partial t} + \mathbf{u} \cdot \nabla n - \nabla^2 n + S \nabla \cdot (r(c)n \nabla c) &= f_n, \end{aligned} \quad (18)$$

$$\frac{\partial c}{\partial t} + \mathbf{u} \cdot \nabla c - Le_\tau \nabla^2 c = Hnr(c) + f_c \text{ in } \Omega.$$

The physical properties are set at the constant values of $Pr_\tau = S = r(c) = Le_\tau = H = 1$ and $Ra_\tau = 1$ or $Ra_\tau = 2000$ in $\Omega = [0, 1] \times [0, 1]$. The cutoff value c^* is neglected here and \mathbf{f}_u , f_n , and f_c are derived such that $u_{\text{exact}} = -\cos(\pi x) \sin(\pi y) e^{-2\pi^2 t}$, $v_{\text{exact}} = \sin(\pi x) \cos(\pi y) e^{-2\pi^2 t}$, $p = c_1 - 0.25(\cos(2\pi x) + \cos(2\pi y)) e^{-4\pi^2 t}$, $n_{\text{exact}} = \cos(\pi x) \cos(\pi y) e^{-2\pi^2 t}$, and $c_{\text{exact}} = \cos(\pi x) \cos(\pi y) e^{-2\pi^2 t}$ are the exact solutions to (18). Such a cell-density solution decays to zero. Equations in (18) are solved with no-slip boundary conditions for \mathbf{u} and homogeneous Neumann boundary condition for c and n with $\Delta t = 0.0001$ in the continuously refined four meshes with $\Delta x = \Delta y = 0.125, 0.1, 0.0625, 0.05$. The predicted errors between the simulated and exact solutions are cast in their L_2 -norms. From the predicted error norms, the spatial rates of convergence are plotted in Fig. 2.

The good agreement between the exact and simulated results and states of convergence demonstrate the applicability of the proposed SUPG scheme and the flow solver described in Section 3.2 to investigate the chemotactic phenomena in hydrodynamic environment.

4. Numerical results and discussion

The linear stability analysis of the system (11) showed that the steady state becomes unstable for a range of physical parameters [2]. For sufficiently large characteristic bacterial density \bar{n}_0 and Rayleigh number Ra_τ , hydrodynamic instabilities appear in the region near the surface at which the bacterial density is high. This instability may be related to the Rayleigh–Bénard instability occurring in thermal convection [3,17]. This instability develops into a descending family of bacterium-rich plumes and leads possibly to the formation of convection cells (Fig. 3(a)).

When \bar{n}_0 is small, small perturbations of the velocity field are damped due to stabilizing effects of viscous friction and chemotaxis and therefore convective motion is negligible. It is shown that for low

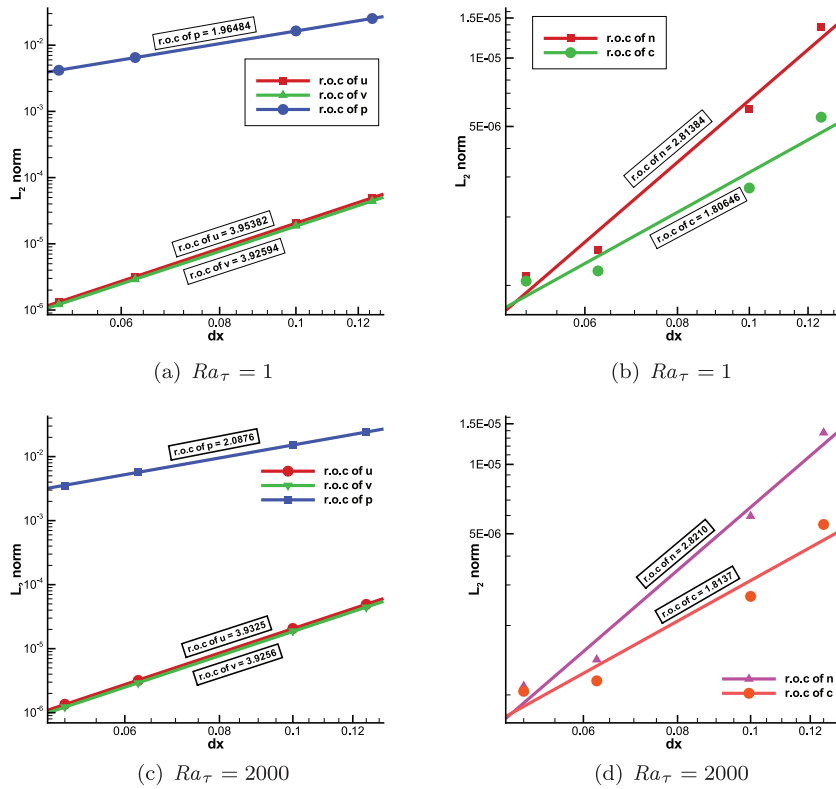


Fig. 2. The computed rates of convergence (roc) for the coupled set of Navier–Stokes and Keller–Segel equations at $t = 0.01$ with $Pr_\tau = S = r(c) = Le_\tau = H = 1$.

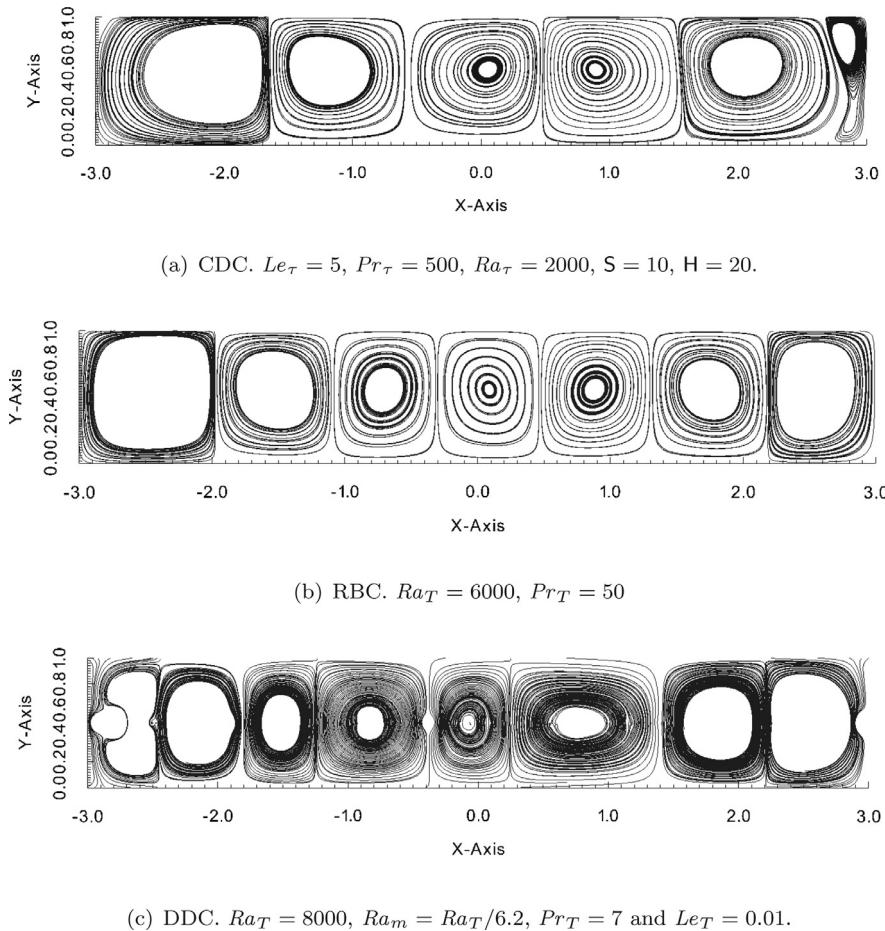


Fig. 3. Examples of convection cells for the chemotaxis–diffusion–convection (CDC) system (11), Rayleigh–Bénard convection (RBC) system (27), and double diffusive convection (DDC) system (27).

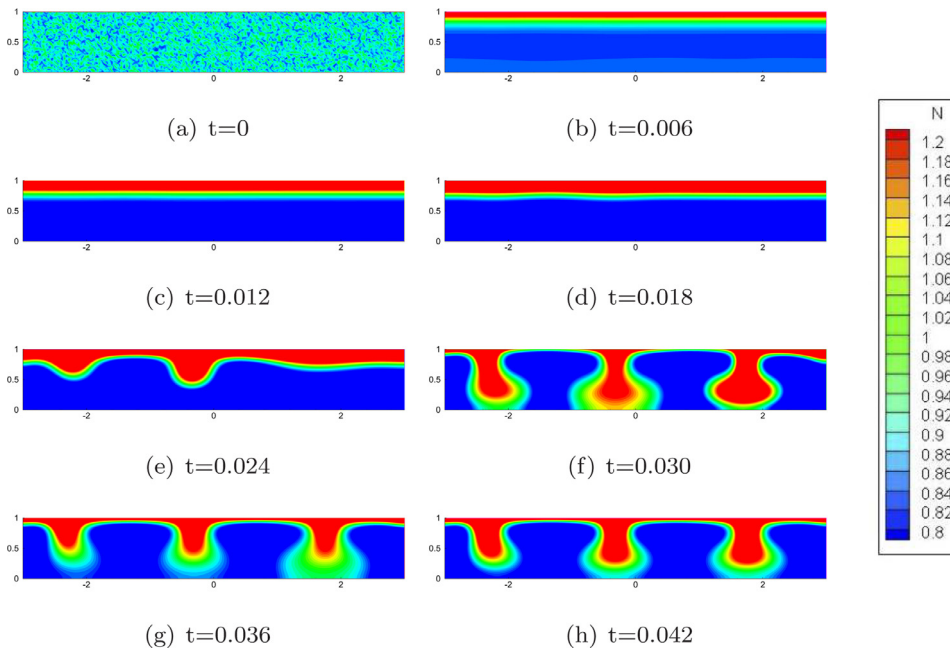


Fig. 4. Evolution of the cell density n at different times. Descending plumes of bacteria develop from an initial randomly distributed bacterium population.

initial bacterium cell density \bar{n}_0 the system (11) evolves to a steady and homogeneous state in the horizontal direction governed by the chemotaxis system [3,21]. Like in the Keller–Segel or angiogenesis system, the random diffusion of cells in this case is balanced by the chemotaxis sensitivity of cells.

4.1. Descending plumes

In the present numerical simulations, the descending plumes can be described using three phases. In the first phase (Fig. 4(a)–(c)), chemotaxis is a dominant mechanism. As bacteria consume oxygen, an oxygen concentration gradient is created that in turn provokes a bacterium motion toward the open surface where the oxygen is abundant. Bacteria chemotaxis causes the fluid to set in motion and counter rotating vortices to form (Fig. 3(a)). Quickly, the bacterial density n becomes quasi-homogeneous in the horizontal direction and is structured in layers in the vertical direction. A three-layer configuration is induced. A layer of higher concentration of bacteria forms below the air surface: the *stack layer*. When bacteria have migrated in the stack layer, a *depletion layer* is generated. At the container bottom, some bacteria may be inactive, because the oxygen concentration decreases below a certain threshold. An *inactive layer* is established. In Fig. 4, the *inactive layer* is not observed at times larger than $t = 0.006$.

The second phase (Fig. 4(d)–(e)) exhibits high bacterial density on the surface. As bacteria swim toward air-supply region, the bacterial density in the stack layer increases. Consequently, advection from the counter rotating vortices becomes significant and strengthens perturbations in the stack layer (Fig. 5) due to lateral flow near the surface. These small perturbations in the cell density can arise from many different sources such as gyrotaxis.

In the third phase (Fig. 4(f)–(h)), in fluid regions with a greater bacterial density in the stack layer, buoyancy force constrains bacteria to descend in the fluid. Local maxima at the surface form due to lateral flow at the surface. As a result of an increased cell density, the observed descending plumes of bacteria develop at these particular locations. However, in Fig. 5, the bacterial density at $t = 0.36$ is indeed larger than that at time $t = 0.30$ due to the chemotactic force strengthening while buoyancy force diminishes at the surface.

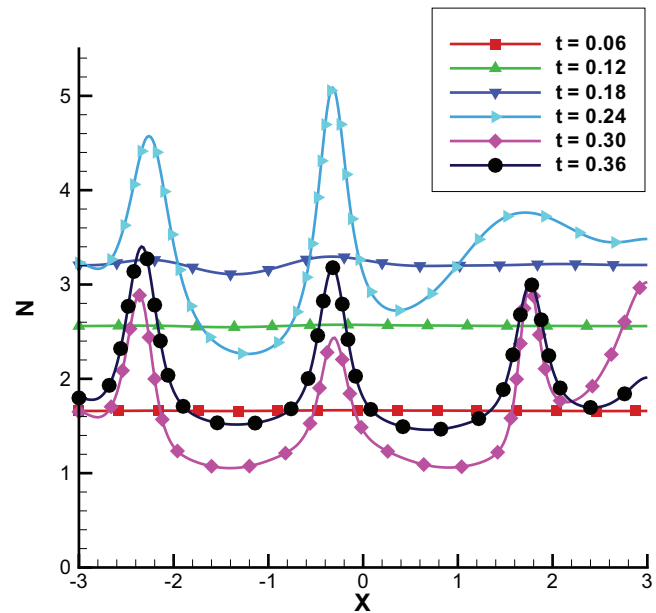


Fig. 5. Evolution of the cell density number n at the surface. In the initial stage of the chemotaxis–diffusion–convection, n is homogeneous in the horizontal direction. As the cell density n increases, hydrodynamic instability arises and the bacterial density becomes higher at some particular points due to lateral flow at the surface. Positions of the plumes correspond to the positions of the plumes in Fig. 4.

This mechanism is analogous to the Rayleigh–Bénard instability in heat transfer problems where the fluid with a higher temperature and thus a lighter density than that above it rises to develop plumes of hot fluid.

4.2. Stabilizing effect of chemotaxis

When the average initial cell density \bar{n}_0 is large, hydrodynamic instabilities appear in the system (11). This section is aimed at estimating \bar{n}_0 and dimensionless governing parameters for hydrodynamic instabilities to appear as well as at analyzing the time scales

Table 3

Phenomenological analysis is based on time scales of the three competitive mechanisms: chemotaxis, diffusion, and convection of bacteria. In each of the three cases, the non-dominant mechanisms are non-null and play important role in pattern formation. Both oxygen and bacterial diffusion favor fluid homogenization.

Dominant convection	Dominant diffusion	Dominant aerotaxis
$T_{\text{conv}} < T_{\text{diff}}$ and $T_{\text{conv}} < T_{\tau}$; i.e., $Ra_{\tau} > 1$ and $Ra_{\tau} / SH > 1$	$T_{\text{diff}} < T_{\tau}$ $SH < 1$	$T_{\tau} < T_{\text{diff}}$ $SH > 1$

for each of the three competitive physical mechanisms: (1) chemotaxis, (2) diffusion, and (3) convection of bacteria. In this section, the effects of the geometry are neglected and, for simplicity, the cut-off function is not considered.

Convection is determined by the properties of the hydrodynamic system as well as the container height and \bar{n}_0 via the taxis Rayleigh number Ra_{τ} . When the Rayleigh number is below the critical value for the hydrodynamic system of interest, motion of bacteria is primarily governed by diffusion and chemotaxis with a continuous external oxygen supply; when the Rayleigh number exceeds a critical value, bacterial taxis is primarily caused by gravitation and sustained by continuous external oxygen supply [2].

Buoyancy force enables a fluid volume with a low bacterial density to ascend and a fluid volume with a high bacterial density to descend. Nevertheless, bacterium chemotaxis and friction dampen altogether the displacement.

The time scale for bacterium diffusion over the length scale h is given by

$$T_{\text{diff}} := \frac{h^2}{D_b}. \quad (19)$$

The buoyancy force is balanced by friction in the fluid. Therefore, the time scale for the convective displacement of bacteria over the length scale h can be defined by

$$T_{\text{conv}} := \frac{\mu}{gh \bar{n}_0 V_b (\rho_b - \rho)}. \quad (20)$$

The chemotaxis system is controlled by a competition between diffusion and chemotaxis of bacteria. Therefore, the chemotaxis time scale is expressed as

$$T_{\tau} := \frac{D_b}{S_{\text{dim}} \kappa \bar{n}_0}. \quad (21)$$

In a convection-dominant process, the convection time scale is smaller than the diffusion and chemotaxis time scales. Hence:

$$\frac{gh^3 \bar{n}_0 V_b (\rho_b - \rho)}{D_b \mu} \equiv Ra_{\tau} > 1. \quad (22)$$

In particular, $Ra_{\tau} > Ra_c$. The value of the critical Rayleigh number associated with the convection Ra_c given by [2] in their linear stability analysis is described by the solution of an ordinary differential system. The second condition on the time scales leads to the following inequality

$$\frac{gh D_b V_b (\rho_b - \rho)}{S_{\text{dim}} \kappa \mu} \equiv \frac{Ra_{\tau}}{SH} > 1. \quad (23)$$

On the other hand, the chemotactic motion is predominant when the chemotaxis time scale is smaller than the diffusive time scale and convection is negligible:

$$\frac{S_{\text{dim}} \kappa \bar{n}_0 h^2}{D_b^2} \equiv SH > 1. \quad (24)$$

Table 3 summarizes the phenomenological analysis based on time scales of the three competitive mechanisms: chemotaxis, diffusion,

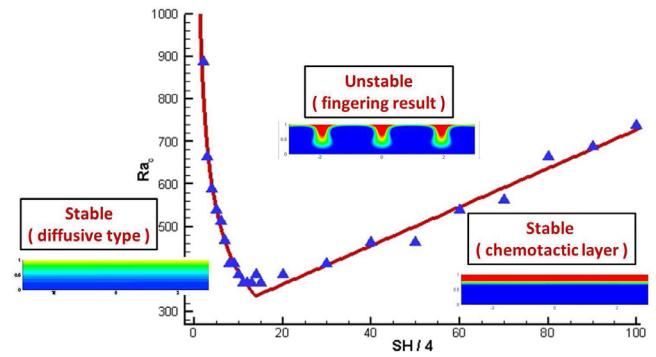


Fig. 6. The stable and unstable regions of the system (11) are plotted in terms of the critical taxis Rayleigh number Ra_c and the product of the dimensionless chemotaxis sensitivity and chemotaxis head SH . The points correspond to the predicted values of Ra_c . The red line corresponds to a fit of data in two parts: on the left side of the point where the minimum value of Ra_c is reached, the points are fitted by a power function and on the right side by a linear function. In the unstable region, the predicted solution n is of the convective type. In the stable region the predicted solution n can be of the diffusive type or the chemotactic type. (For interpretation of the references to color in this figure legend, the reader is referred to the web version of this article.)

and convection of bacteria. In each of the three cases, the non-dominant mechanisms are non-null. In the convection dominant case, both chemotaxis and diffusion occur in the sequence described in Section 4.1. In this phenomenological analysis, the cut-off function is neglected ($r(c) = 1$) and the effects of the geometry are only taken into account through the length scale that corresponds to the height of the domain.

The effects of Ra_c and the product SH were tested subject to the random initial condition. S_{dim} and κ are used to vary SH . The results are shown in Fig. 6 for $Pr_{\tau} = 500$ and $Le_{\tau} = 5$. Our numerical results agree with the linear stability analysis carried out in [2]. Ra_c at first falls as SH increases to reach its minimum value and then rises again. A sufficient decrease or increase of SH may promote stabilization as both taxis and diffusion operate as the fluid-homogenization factors, either directly ($SH < 1$) or indirectly ($SH > 1$). When SH is small, stabilizing effect is due to bacterial diffusion and the solution is of the diffusive type. When SH is large, stabilizing effect results from the bacterial taxis and the solution is of the chemotactic type.

The taxis Rayleigh number (Ra_{τ}) that characterizes the competition between diffusion and convection plays the same role as the Rayleigh number plays in classical convection. When the Rayleigh number increases, the gravitational force becomes predominant. When SH rises, competition between chemotaxis and convection of bacteria becomes stronger. The condition (23) suggests that Ra_c increases linearly with respect to SH , as illustrated in Fig. 6. We can affirm that chemotaxis has a stabilizing effect on the differential system of current interest.

4.3. Distribution and number of plumes and initial conditions

4.3.1. Position and spacing of plumes

The exact localization of plume generation was investigated. The random initial condition introduced in [21] does not introduce an internal length scale but difficulties arise to predict the plume locations. We then consider a set of deterministic initial conditions to investigate the location of descending plumes. Deterministic initial conditions have the advantage of making possible to analyze and compare the obtained numerical results.

The parameters for all computed numerical results are chosen as those in [21] to ensure the formation of bacterium rich plumes: $Le_{\tau} = 5$, $Pr_{\tau} = 500$, $Ra_{\tau} = 2000$, $S = 10$, and $H = 4$. Numerical results are shown in Figs. 7–10 at time $t = 1.2$ when the observed

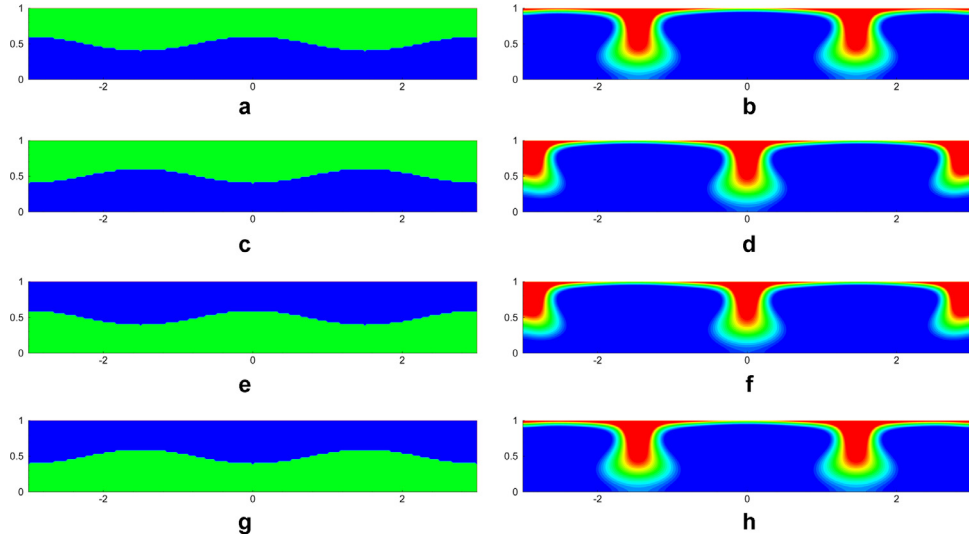


Fig. 7. Numerical results for n at time $t = 1.2$ (right) with respect to the corresponding deterministic initial conditions (left). In (a) and (c), $n = 1$ in the upper layer and $n = 0.5$ in the lower layer. In (e) and (g), $n = 1$ in the lower layer and $n = 0.5$ in the upper layer.

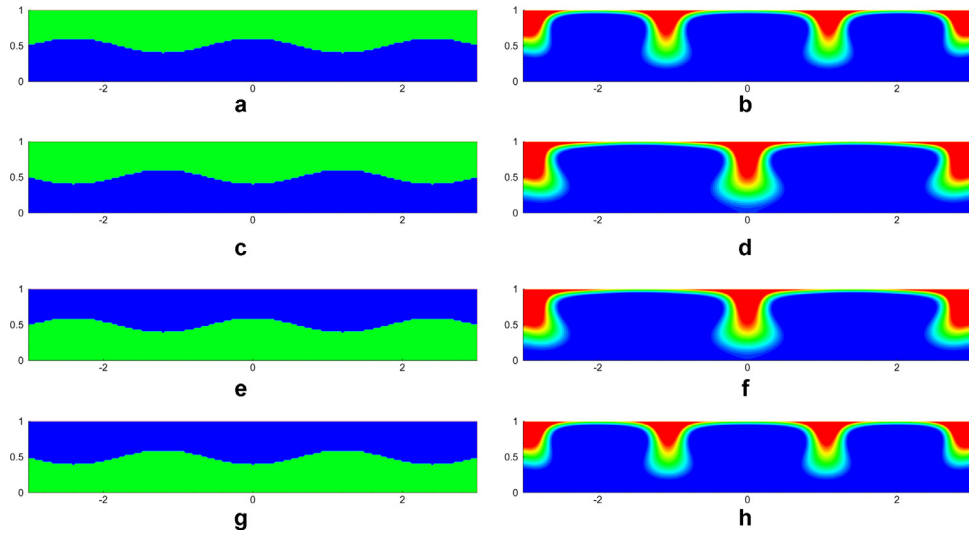


Fig. 8. Numerical results for n at time $t = 1.2$ (right) with respect to the corresponding deterministic initial conditions (left). In (a) and (c), $n = 1$ in the upper layer and $n = 0.5$ in the lower layer. In (e) and (g), $n = 1$ in the lower layer and $n = 0.5$ in the upper layer.

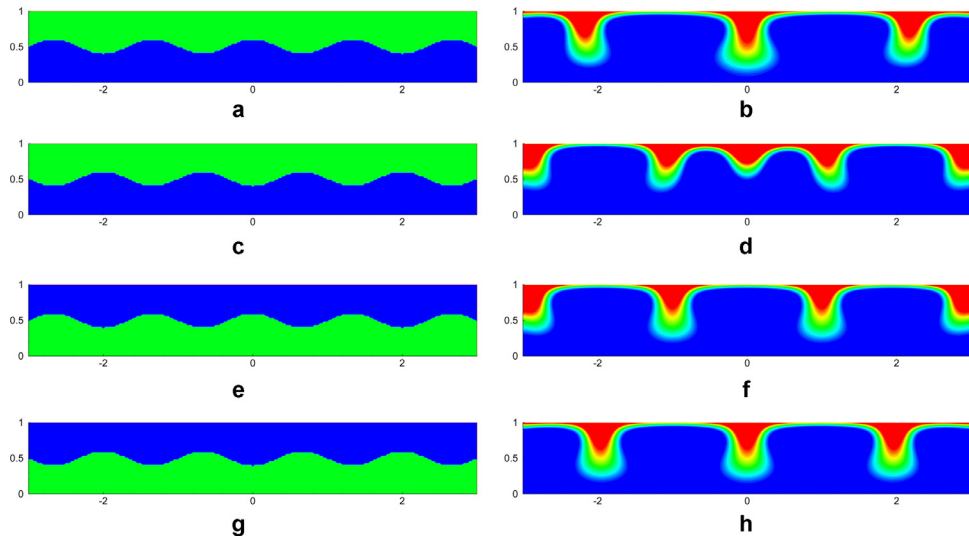


Fig. 9. Numerical results for n at time $t = 1.2$ (right) with respect to the corresponding deterministic initial conditions (left). In (a) and (c), $n = 1$ in the upper layer and $n = 0.5$ in the lower layer. In (e) and (g), $n = 1$ in the lower layer and $n = 0.5$ in the upper layer.

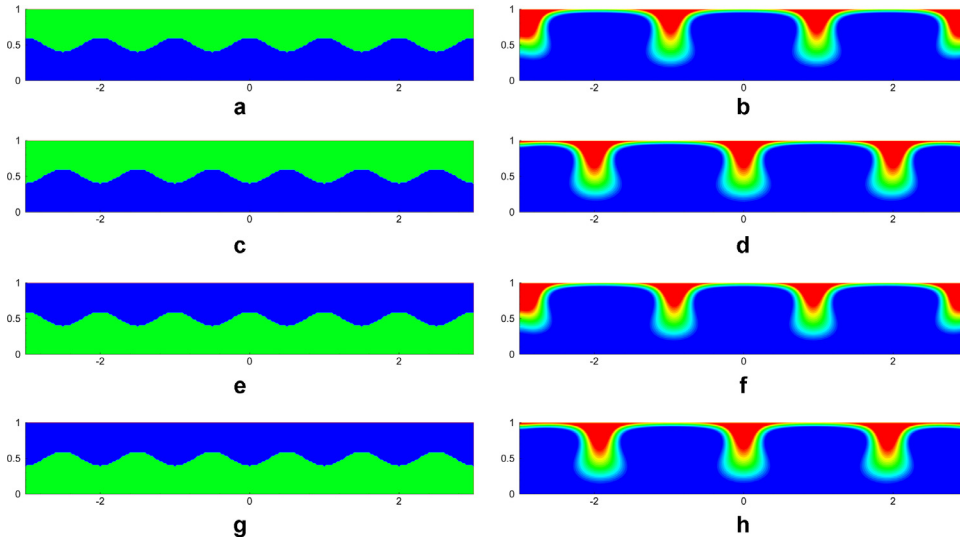


Fig. 10. Numerical results for n at time $t = 1.2$ (right) with respect to the corresponding deterministic initial conditions (left). In (a) and (c), $n = 1$ in the upper layer and $n = 0.5$ in the lower layer. In (e) and (g), $n = 1$ in the lower layer and $n = 0.5$ in the upper layer.

descending plumes are fully formed but the solution has not yet reached the numerically stationary state.

We first consider a profile given by the form of wave function $\cos(2\pi x/3)$ to determine the two initial layers of bacteria. Simulation results and initial conditions are shown in Fig. 7. The upper layer has a higher bacterial density than the lower layer. The plumes form at the initial location of the crest of the wave function where there is a larger number of bacteria. By reversing the initial conditions with a denser inferior layer, the plumes also form at the same location. We can observe that distinct initial conditions can lead to the formation of a very similar pattern (Fig. 7).

We vary the profile of the curve between the upper and lower layers in the initial condition with different wave functions $\cos(3\pi x/2)$, $\cos(5\pi x/2)$, and $\cos(2\pi x)$ (Figs. 8–10). The wavenumber is defined as the spatial frequency of waves per unit distance. The wavelength is defined as the domain horizontal length divided by the wavenumber. Increasing the wavenumber of the initial wave function causes the formation of additional plumes to occur (Fig. 8). In all simulations, the locations of the plumes correspond to sites of initially greater local bacterial density.

When the wavenumber in the initial profile is large enough, the number of plumes is not equal to the wavenumber fixed by the initial condition. Three plumes, at most, form (Figs. 9 and 10). Nonetheless, more than three plumes can form, but they merge later (Fig. 10). Plume merging was previously observed in [21]. The plume merging mechanism is analogous to that of the Rayleigh–Bénard flow. Spacing between plumes seems to be intrinsic to the system and the position can only be predicted in very specific cases such as the examples given above.

The randomly perturbed bacterial density is defined as follows [21]:

$$n(x) = 0.8 + 0.2\varepsilon(x), \quad (25)$$

with ε being a random number with a uniform probability distribution over $[0, 1]$. Simulation results with the randomly perturbed initial condition are given in Fig. 11. We note that the plume-to-plume spacing is not fixed but the number of plumes in the solution remains the same as that with the solution obtained subject to the deterministic initial condition illustrated in Figs. 9 and 10. Plume-to-plume spacing also depends on the geometry of the domain.

In Figs. 7–11, we can see plumes forming at the border of the domain. These border plumes seem to be caused by the no-slip boundary condition on the velocity depending on the arrangement of the

convection cells. Bacteria first agglomerate at the surface near the wall. Because the fluid velocity is equal to zero at the wall boundary, a large amount of bacteria remains close to the wall. At a location away from the wall, the velocity is non-zero, thus bacteria descend into the fluid and form a plume at the border.

The location of the plumes may only be predicted in very simple tests for which the wavelengths of initial conditions are lower than the wavelength of the process. Despite the difficulty to predict the site of plume formation, the system presents a dominant wavelength of the fingering instability. The wavelength and wavenumber are defined such as in [31]. The wavelength is the length of the domain divided by the number of plumes and the wavenumber 2π divided by the wavelength. The wavelength and wavenumber are similar for all simulation tests whatever the length of the domain is. The number of plumes is given at $t = 1.2$ (Table 4). Merging of plumes can occur so that a different number of plumes can be observed for a given ℓ .

4.3.2. Growth of plumes

We now arbitrarily define the plumes by the isoline $n = 1$ in dimensionless variable. This choice allows us to track the stack layer and the plumes being formed. The layer where $n > 1$ represents the layer with a high bacterial density from which plumes form and descend in the fluid. On the other hand, the layer with $n < 1$ corresponds to the depletion layer, from which bacteria have migrated to the stack layer.

We define the growth rate of the plume amplitudes by $G = (A_t - A_{t-1})/\Delta t$. The plume amplitude A_t is computed by measuring the distance from the surface to the tip of the plume at time t (Table 5) and Δt denotes the time step used for numerical simulations. Δt has been chosen to be small enough so that the plume patterns can be observed numerically. Data obtained can be interpolated by the exponential function $g(t) = \exp\{\alpha t + \beta\}$ until the descending plumes reach three quarters of the domain height (Fig. 12). The exponential growth is well understood in the conventional Rayleigh–Taylor convection. Subsequent to the exponential growth phase, the growth rate of amplitude decreases, as plumes get closer to the bottom of the container.

4.4. Comparison with other buoyancy-driven convections

The chemotaxis–diffusion–convection system has many features similar to other well known buoyancy-driven flows, such as the double diffusive and Rayleigh–Bénard convection.

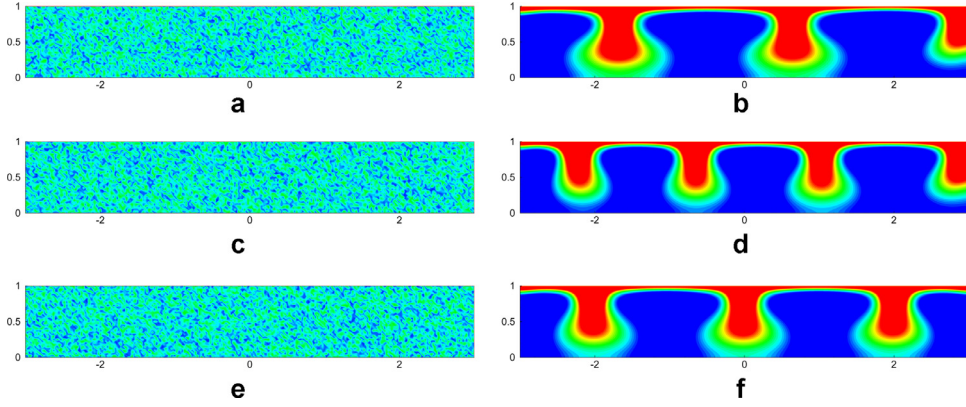


Fig. 11. Simulations subject to the initial condition given in (25) (left) and the corresponding numerical results for n at $t = 1.2$ (right).

Table 4

The predicted number of plumes, wavenumber and wavelength for different values of ℓ . Each simulation result are subject to the randomly perturbed initial condition given in (25).

ℓ	Number of plumes	Wavelength	Wavenumber	Frequency
2	2	2	3.14	Four out of four times
3	3	2	3.14	Three out of four times
3	4	1.5	4.19	One out of four times
4	5	1.6	3.93	Four out of four times
5	5	2	3.14	Three out of four times
5	6	1.67	3.77	One out of four times

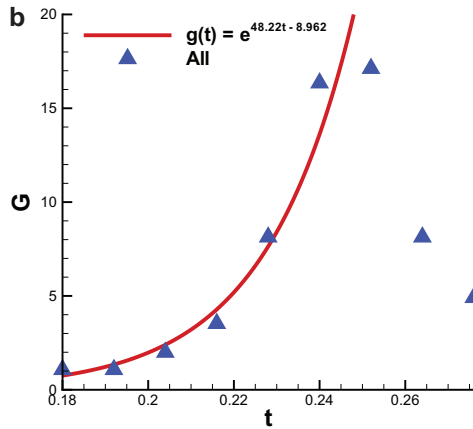
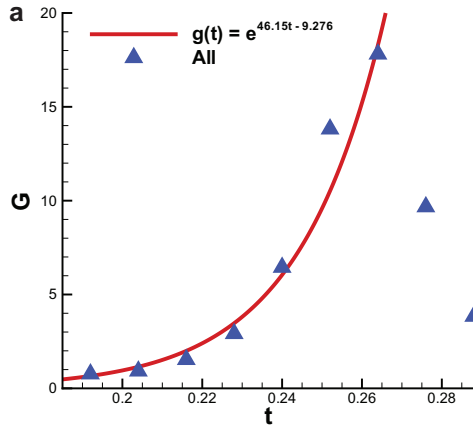


Fig. 12. Plot of the growth rate G of plume amplitude (dots) corresponding to the data in Table 5. The growth rate is interpolated by the exponential function $g(t) = e^{\alpha t + \beta}$ (line).

Table 5

The predicted growth rate G of the plume amplitudes A_t for two simulations subject to the random initial condition (25).

(a)			(b)		
A_t	t	G	A_t	t	G
0.18	0.168		0.18	0.168	
0.19	0.180	0.46	0.20	0.180	1.07
0.20	0.192	0.76	0.21	0.192	1.07
0.21	0.204	0.92	0.23	0.204	1.99
0.23	0.216	1.53	0.28	0.216	3.53
0.26	0.228	2.91	0.37	0.228	8.13
0.34	0.240	6.44	0.57	0.240	16.34
0.51	0.252	13.81	0.78	0.252	17.12
0.72	0.264	17.81	0.87	0.264	8.13
0.83	0.276	9.67	0.93	0.276	4.91

Double diffusive convection occurs in a fluid containing at least two components with different diffusivities. A destabilizing component diffuses faster than the stabilizing one [32]. The distinct diffusivities yield a density difference capable of driving the motion of fluid [33].

Comparison with a classical example of double diffusive phenomenon in oceanography can be carried out by considering two superposed fluid layers with a specific combination of temperature (T) and the solute concentration (s), namely the salinity. The system of dimensionless equations of the double diffuse problem is the following:

$$\begin{aligned}
 \frac{\partial \mathbf{u}}{\partial t} + (\mathbf{u} \cdot \nabla) \mathbf{u} - Pr_T \nabla^2 \mathbf{u} + Pr_T \nabla p &= -Pr_T (Ra_m s - Ra_T T) \mathbf{j}, \\
 \nabla \cdot \mathbf{u} &= 0, \\
 \frac{\partial T}{\partial t} + \mathbf{u} \cdot \nabla T - \nabla^2 T &= 0, \\
 \frac{\partial s}{\partial t} + \mathbf{u} \cdot \nabla s - Le_T \nabla^2 s &= 0,
 \end{aligned}
 \tag{26}$$

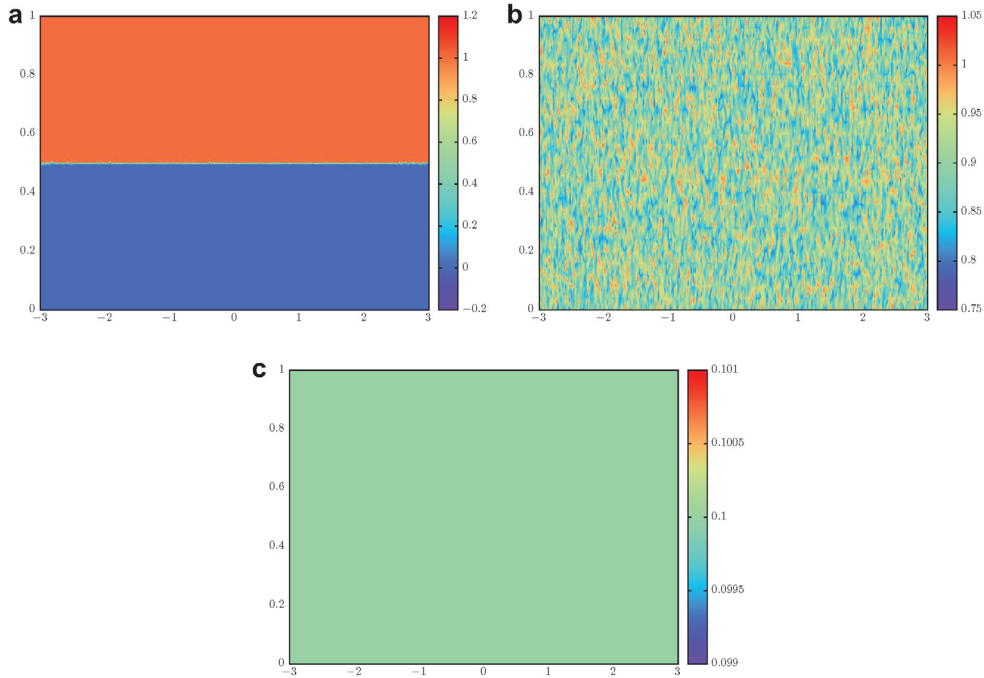


Fig. 13. Initial concentration and temperature profiles for, from left to right, the double diffusive convection system (26), the chemotaxis–diffusion–convection system (10), and temperature profile for the Rayleigh–Bénard convection system (27), respectively. (Left) Initial concentration $s(x, y, t = 0) = 2/7$, if $y < 0.5$, and $s(x, y) = 1.0$, if $y \geq 0.5$. (Center) Randomly generated concentration $n \in [0.8, 1]$. (Right) Initial temperature profile $T = 0.1$.

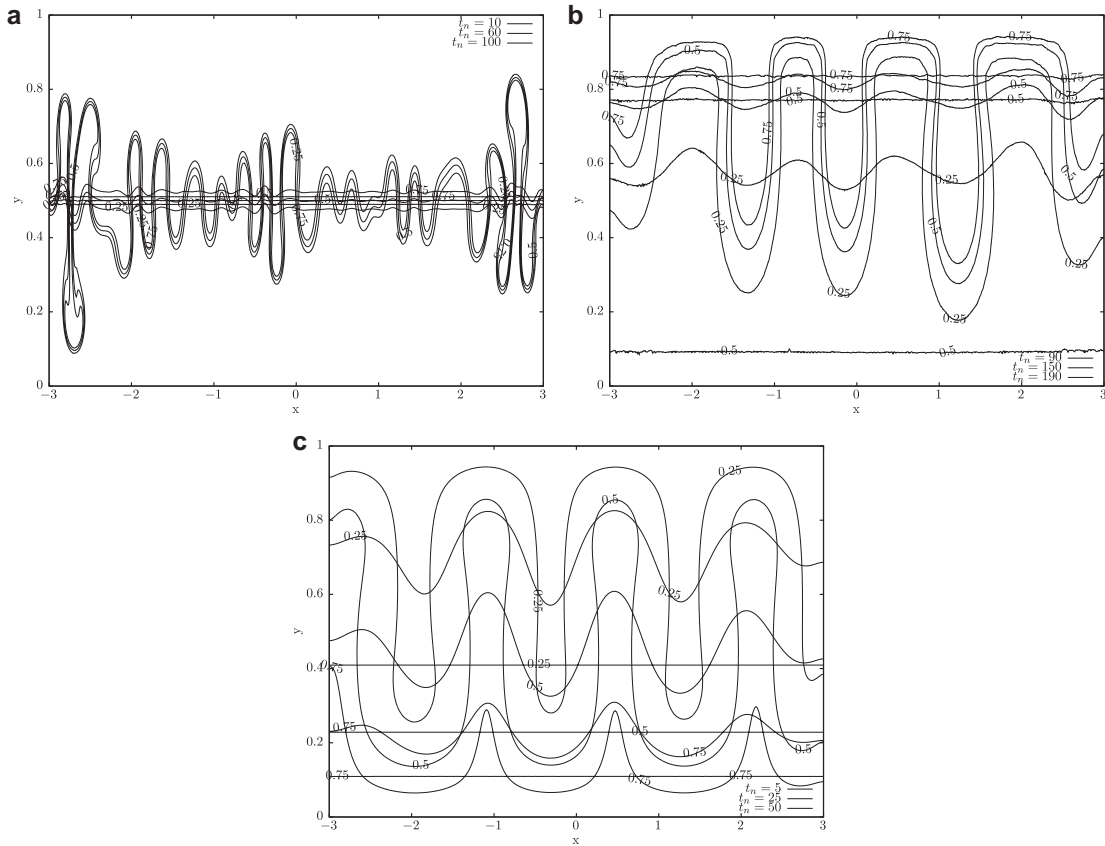


Fig. 14. Concentration and temperature contours at different times for, from left to right, the double diffusive convection system (26), the chemotaxis–diffusion–convection system (10), and temperature profile for the Rayleigh–Bénard convection system (27), respectively. In the three cases, fingers develop with time. (Left) $Ra_T = 8000$, $Ra_m = Ra_T/6.2$, $Pr_T = 7$ and $Le_T = 0.01$. (Center) $Le_T = 5$, $Pr_T = 500$, $Ra_T = 2000$, $S = 10$, and $H = 20$. (Right) $Ra_T = 6000$, $Pr_T = 50$.

Table 6
Recapitulative of the physical mechanisms involved in the double diffusive convection (DDC), chemotaxis–diffusion–convection (CDC) and the Rayleigh–Bénard convection (RBC).

	DDC	CDC	RBC
Hydrodynamics buoyancy (ρVg)	$\nabla \cdot \mathbf{u} = 0$ $\frac{D\mathbf{u}}{Dt} = Pr_T \nabla^2 \mathbf{u} - Pr_T \nabla p$ $-Pr_T (Ra_m s - Ra_T T) \mathbf{j}$	$\nabla \cdot \mathbf{u} = 0$ $\frac{D\mathbf{u}}{Dt} = Pr_\tau \nabla^2 \mathbf{u} - Pr_\tau \nabla p$ $-Ra_\tau Pr_\tau n \mathbf{j}$	$\nabla \cdot \mathbf{u} = 0$ $\frac{D\mathbf{u}}{Dt} = Pr_T \nabla^2 \mathbf{u} - Pr_T \nabla p$ $-Pr_T Ra_T \mathbf{j}$
Diffusion	$\frac{DT}{Dt} = \nabla^2 T$ $\frac{Ds}{Dt} = Le_T \nabla^2 s$	$\frac{Dn}{Dt} = \nabla^2 n$	$\frac{DT}{Dt} = \nabla^2 T$
Chemotaxis	\emptyset	$\frac{Dn}{Dt} = -S \nabla \cdot (n \nabla c)$ $\frac{Dc}{Dt} = Le_c \nabla^2 c - Hn$	\emptyset
Convection	$\frac{DT}{Dt} = \mathbf{u} \cdot \nabla T$ $\frac{Ds}{Dt} = \mathbf{u} \cdot \nabla s$	$\frac{Dn}{Dt} = \mathbf{u} \cdot \nabla n$	$\frac{Dn}{Dt} = \mathbf{u} \cdot \nabla n$
I.C. for fingers	Layers	Any	Layers
B.C. for mass	Neumann	Neumann	Dirichlet
Physical regime	Diffusive and convective	Diffusive, convective and chemotactic	Diffusive and convective

where Ra_T and Ra_m are the thermal and mass Rayleigh number, respectively, Pr_T the Prandtl number, and Le_T the Lewis number (Table 2).

The stability of the system that exhibits a diffusive and a finger regime depends on both Rayleigh number types. In the finger regime, a small perturbation at the interface between the layers develops into a pattern of descending fingers, for instance salt fingers.

Another buoyancy-driven convection is the Rayleigh–Bénard convection that arises by fluid in a reservoir heated from below. Convection results from thermal gradient. The set of equations is as follows:

$$\begin{aligned} \frac{\partial \mathbf{u}}{\partial t} + (\mathbf{u} \cdot \nabla) \mathbf{u} - Pr_T \nabla^2 \mathbf{u} + Pr_T \nabla p &= -Pr_T Ra_T T \mathbf{j}, \\ \nabla \cdot \mathbf{u} &= 0, \\ \frac{\partial T}{\partial t} + \mathbf{u} \cdot \nabla T - \nabla^2 T &= 0, \end{aligned} \tag{27}$$

$$T = 1 \text{ at bottom, } T = 0 \text{ at top.}$$

Ra_T and Pr_T are the Rayleigh and Prandtl number, respectively. The balance between the gravitational and viscous forces is expressed by the Rayleigh number Ra_T . When Ra_T is larger than a critical value that can be obtained analytically, convective patterns appear [34].

The double diffusive convection equations in (26) and the Rayleigh–Bénard convection equations in (27) are solved using our numerical method. Initial conditions and evolution in time of concentration profiles are plotted in Figs. 13 and 14, respectively. Plumes formed in the Rayleigh–Bénard convection process are similar in shape to plumes of the chemotaxis–diffusion–convection. However, double diffusive and Rayleigh–Bénard convections exhibit both ascending and descending plumes, whereas chemotaxis–diffusion–convection exhibits descending plumes.

In each problem, the effective Rayleigh numbers depend on the temperature difference between the opposite fluid domain surfaces, the gradients of temperature and salinity between the fluid layers, and the difference of density between the bacteria and solvent, for the Rayleigh–Bénard, double diffusive, and chemotaxis–diffusion–convection systems, respectively. All of the three diffusion–convection processes have similar and distinct features (Table 6). The involved dimensionless parameters are listed in Table 2.

Fig. 3 shows that the arrangement of the convection cell structure can be the same for the three systems mentioned above. A particular position of the domain will be in a clockwise cell in some simulations and counter-clockwise cell in others. This behavior is also observed in Rayleigh–Bénard convection simulations.

The presented chemotaxis–diffusion–convection system is also characterized by gravity and the continuous feeding of oxygen. Chemotaxis driven by the continuous feeding of oxygen plays essential role in the early stage, as it organizes the fluid domain. In a rectangular domain, starting from a given initial condition, aerotaxis of bacteria builds quasi-homogeneous layers in the horizontal direction, similarly to the double diffusive case [33]. The multi-layered fluid creates a density gradient between the top of the stack layer and the bottom of the depletion layer that is similar to the temperature gradient set by the Dirichlet boundary condition imposed in the Rayleigh–Bénard case. The chemotaxis–diffusion–convection system evolves itself to a proper condition that leads to instabilities.

Chemotaxis, that is not present in the other systems, brings flexibility in the choice of initial as well as boundary conditions. An analogy between the differential systems should stimulate further mathematical analysis of the system and a better understanding of the role of chemotaxis in convection problems.

5. Concluding remarks

In this paper, we have studied the chemotaxis–diffusion–convection system with the focus on the differential system rather than on the experimental settings. Our studies are based on the numerical implementation of the upwind finite element method with inconsistent Petrov–Galerkin weighted residual scheme to solve the coupled convective chemotaxis–fluid equations. Several simulation examples have been presented. They exhibit physically different spatially organized convection patterns.

The chemotaxis–diffusion–convection system can be described by three regimes. In the convective regime, the formation of plume patterns proceeds a temporal sequence of development stages. First, a spatial layered structure is created. Bacteria agglomerate in the upper stack layer, thus forming a depletion layer, where the bacterial density is very low. Subsequently, bacterial convection strengthens with time and instabilities in the stack layer appear. Finally, plumes of bacterial falling in the fluid are generated. The growth rate of the plumes is of the exponential type. The wavelength of the growing instabilities is defined from the parameters of the problem. Initial conditions appear to have a small influence on the plume number. The location of plumes can only be predicted when a very simple initial condition is set up.

In the diffusive and chemotactic regimes, the chemotaxis system has a stabilizing effect on the stack layer and thus suppresses its instability. When the taxis Rayleigh number increases, the gravitational force becomes dominant and instabilities occur and

grow. From the phenomenological analysis and the numerical results, the critical Rayleigh number increases proportionally with the product of the chemotaxis sensitivity and head, when the chemotaxis sensitivity is large.

In all buoyancy-driven flows (chemotaxis–diffusion, double diffusive, and Rayleigh–Bénard convection), the dimensionless differential systems and the convection patterns are similar. Analogy between these types of convection should launch further analytical studies of the chemotaxis–diffusion–convection problem.

Acknowledgments

Y.D. received a Ph.D. grand from Pierre and Marie Curie University – Sorbonne University and was also supported by the CASTS at National Taiwan University.

References

- [1] Brenner MP, Levitov LS, Budrene EO. Physical mechanisms for chemotactic pattern formation by bacteria. *Biophys J* 1998;74(4):1677–93.
- [2] Hillesdon AJ, Pedley TJ. Bioconvection in suspensions of oxytactic bacteria: linear theory. *J Fluid Mech* 1996;324(10):223–59.
- [3] Hillesdon AJ, Pedley TJ, Kessler JO. The development of concentration gradients in a suspension of chemotactic bacteria. *Bull Math Biol* 1995;57(2):299–344.
- [4] Hill N, Pedley T. Bioconvection. *Fluid Dyn Res* 2005;37(1–2):1–20.
- [5] Keller EF, Segel LA. Model for chemotaxis. *J Theor Biol* 1971;30(2):225–34.
- [6] Patlak CS. Random walk with persistence and external bias. *Bull Math Biophys* 1953;15(3):311–38.
- [7] Blanchet A, Dolbeault J, Perthame B. Two-dimensional Keller–Segel model: optimal critical mass and qualitative properties of the solutions. *Electron J Differ Equ* 2006;44:1–33.
- [8] Herrero MA, Velázquez JLL. Singularity patterns in a chemotaxis model. *Math Ann* 1996;306(1):583–623.
- [9] Jäger W, Luckhaus S. On explosions of solutions to a system of partial differential equations modelling chemotaxis. *Trans Am Math Soc* 1992;329(2):819–24.
- [10] Nagai T, Senba T. Global existence and blow-up of radial solutions to a parabolic-elliptic system of chemotaxis. *Adv Math Sci Appl* 1998;8:145–56.
- [11] Velázquez JLL. Point dynamics in a singular limit of the Keller–Segel model 2: formation of the concentration regions. *SIAM J Appl Math* 2004;64(4):1224–48.
- [12] Perthame B. Cell motion and chemotaxis. In: *Transport equations in biology*. Basel: Birkhauser; 2007. p. 111–49.
- [13] Chaplain M, McDougall S, Anderson A. Mathematical modeling of tumor-induced angiogenesis. *Ann Rev Biomed Eng* 2006;8(1):233–57.
- [14] Mantzaris NV, Webb S, Othmer HG. Mathematical modeling of tumor-induced angiogenesis. *J Math Biol* 2004;49(2):111–87.
- [15] Corrias L, Perthame B, Zaag H. A chemotaxis model motivated by angiogenesis. *C R Math* 2003;336(2):141–6.
- [16] Corrias L, Perthame B, Zaag H. Global solutions of some chemotaxis and angiogenesis systems in high space dimensions. *Milan J Math* 2004;72(1):1–28.
- [17] Metcalfe A, Pedley T. Bacterial bioconvection: weakly nonlinear theory for pattern selection. *J Fluid Mech* 1998;370:249–70.
- [18] Tuval I, Cisneros L, Dombrowski C, Wolgemuth CW, Kessler JO, Goldstein RE. Bacterial swimming and oxygen transport near contact lines. *Proc Natl Acad Sci USA* 2005;102(7):2277–82.
- [19] Duan R, Lorz A, Markowich P. Global solutions to the coupled chemotaxis–fluid equations. *Commun Partial Differ Equ* 2010;35(9):1635–73.
- [20] Liu J-G, Lorz A. A coupled chemotaxis–fluid model: global existence. *Ann l'Institut Henri Poincaré (C) Nonlinear Anal* 2011;28(5):643–52.
- [21] Chertock A, Fellner K, Kurganov A, Lorz A, Markowich PA. Sinking, merging and stationary plumes in a coupled chemotaxis–fluid model: a high-resolution numerical approach. *J Fluid Mech* 2012;694:155–90.
- [22] Ladyženskaja OA. *The mathematical theory of viscous incompressible flow*. New York: Gordon and Breach Science; 1969.
- [23] Babuška PL. Error-bounds for finite element method. *Numer Math* 1971;16(4):322–33.
- [24] Brezzi F. On the existence, uniqueness and approximation of saddle-point problems arising from lagrangian multipliers. *ESAIM: Math Model Numer Anal* 1974;8(R2):129–51.
- [25] Brooks AN, Hughes TJ. Streamline upwind/Petrov–Galerkin formulations for convection dominated flows with particular emphasis on the incompressible Navier–Stokes equations. *Comput Methods Appl Mech Eng* 1982;32(1–3):199–259.
- [26] Wang MMT, Sheu TWH. Implementation of a free boundary condition to Navier–Stokes equations. *Int J Numer Methods Heat Fluid Flow* 1997;7(1):95–111.
- [27] Sheu TWH, Wang MMT. A comparison study on multivariant and univariant finite elements for three-dimensional incompressible viscous flows. *Int J Numer Methods in Fluids* 1995;21(8):683–96.
- [28] Wang MMT. Development of finite element method for incompressible Navier–Stokes equations (Ph.D. thesis). National Taiwan University; 1996.
- [29] Wang MMT, Sheu TWH. An element-by-element BICGSTAB iterative method for three-dimensional steady Navier–Stokes equations. *J Comput Appl Math* 1997;79(1):147–65.
- [30] Hecht F. New development in FreeFem++. *J Numer Math* 2013;20(3–4):251.
- [31] Pan TW, Joseph DD, Glowinski R. Modelling Rayleigh–Taylor instability of a sedimenting suspension of several thousand circular particles in a direct numerical simulation. *J Fluid Mech* 2001;434:23–37.
- [32] Lemaître L, Budroni MA, Riolfo LA, Grosfils P, Wit AD. Asymmetric Rayleigh–Taylor and double-diffusive fingers in reactive systems. *Phys Fluids* 2013;25(1):014103.
- [33] Turner JS. Double-diffusive phenomena. *Ann Rev Fluid Mech* 1974;6(1):37–54.
- [34] Bodenschatz E, Pesch W, Ahlers G. Recent developments in Rayleigh–Bénard convection. *Ann Rev Fluid Mech* 2000;32(1):709–78.